

# C-RITNet: Set Infrared and Visible Image Fusion Free from Complementary Information Mining

Yafei Zhang<sup>a,b</sup>, Keying Du<sup>a,b</sup>, Huafeng Li<sup>a,b\*</sup>, Zhengtao Yu<sup>a,b</sup>, Yu Liu<sup>c</sup>

*a. Faculty of Information Engineering and Automation, Kunming University of Science and Technology, Kunming 650500, Yunnan, P.R. China.*

*b. Key Laboratory of Artificial Intelligence in Yunnan Province, Kunming University of Science and Technology, Kunming 650500, Yunnan, P.R. China.*

*c. Department of Biomedical Engineering, Hefei University of Technology, Hefei 230009, P.R. China.*

---

## Abstract

Infrared and visible image fusion (IVIF) aims to extract and integrate the complementary information in two different modalities to generate high-quality fused images with salient targets and abundant texture details. However, current image fusion methods go to great lengths to excavate complementary features, which is generally achieved through two efforts. On the one hand, the feature extraction network is expected to have excellent performance in extracting complementary information. On the other hand, complex fusion strategies are often designed to aggregate the complementary information. In other words, enabling the network to perceive and extract complementary information is extremely challenging. Complicated fusion strategies, while effective, still run the risk of losing weak edge details. To this end, this paper rethinks the IVIF outside the box, proposing a complementary-redundant information transfer network (C-RITNet). It reasonably transfers complementary information into redundant one, which integrates both the shared and complementary features from two modalities. Hence, the proposed method is able to alleviate the challenges posed by the complementary information extraction and reduce the reliance on sophisticated fusion strategies. Specifically, to skillfully sidestep aggregating complementary information in IVIF, we first design the mutual information transfer (MIT) module to mutually represent features from two modalities, roughly transferring complementary information into redundant one. Then, a redundant information acquisition supervised by source image (RIASSI) module is devised to further ensure the complementary-redundant information transfer after MIT. Meanwhile, we also propose a structure information preservation (SIP) module to guarantee that the edge structure information of the source images can

---

\*Corresponding author: E-mail: lhchina99@kust.edu.cn

be transferred to the fusion results. Moreover, a mutual promotion training paradigm (MPTP) with interaction loss is adopted to facilitate better collaboration among MIT, RIASSI and SIP. In this way, the proposed method is able to generate fused images with higher qualities. Extensive experiments demonstrate that C-RITNet is superior to state-of-the-art algorithms in terms of visual quality and quantitative evaluations.

*Keywords:* Image fusion, Complementary-redundant information transfer, Mutual representation learning, Mutual promotion training paradigm.

---

## 1. Introduction

Visible light imaging sensors can clearly image objects visible to the human eye, whose imaging results have the advantages of high spatial resolution, rich texture details, and more in line with human visual perception. However, such sensors fail to clearly image objects in severe weather scenes such as fog and haze. Infrared sensors image through measuring the temperature difference between target and background, able to effectively avoid the influence of harsh conditions on target imaging, yet still cannot clearly image the background information with a relatively constant temperature [1]. In order to integrate the advantages of those two types of imaging sensors, infrared and visible image fusion (IVIF) technology is proposed, which can combine the mutual information extracted by the two types of sensors into one image with both clear target and background, achieving a more comprehensive description of the scene. Currently, this technology has been widely used in space exploration, resource exploration, biomedicine, equipment detection, target tracking and other fields.

In recent years, a series of research achievements have been made in infrared and visible image fusion. Effective fusion methods have emerged in large numbers, which can be roughly divided into multi-scale transform-based [2, 3, 4, 5], sparse representation-based [6, 7, 8, 9], and deep learning-based fusion methods [10, 11, 12, 13]. Fusion methods based on multi-scale transform generally perform multi-scale transformation on the source images, then fuse the transform coefficients, and use multi-scale inverse transformation to reconstruct the fusion result. However, multi-scale transformation involved in this type of method often represents the image with a fixed basis, which has weak sparsity and limits the further improvement of fusion performance. In contrast, the sparse representation-based fusion methods can effectively alleviate the above problems by building an over complete dictionary for the represented images from a set of training samples. Nevertheless, it still has weak performance in mining the statistical characteristics of large samples. Deep learning-based methods enjoy high favor among researchers

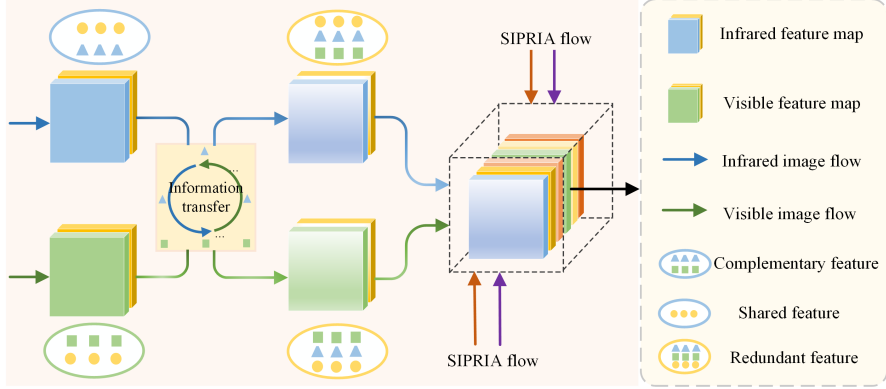


Figure 1: The core idea of our proposed C-RITNet. Redundant feature indicates the shared information of infrared and visible images and modality-specific information from both two modal source images.

lately because they can effectively solve this problem.

At present, numerous excellent deep learning-based IVIF methods have emerged, which are all committed to transferring complementary information from infrared and visible images to the fusion results. Achieving this goal generally requires to make two efforts. On the one hand, the feature extraction network is expected to have excellent performance in complementary information extraction. However, it is extremely challenging for the feature extraction network to effectively perceive complementary information and pay more attention to it. On the other hand, complex fusion strategies are often designed to aggregate the complementary information. In addition, existing fusion schemes all regard redundant information of the source images as meaningless, and strive to ignore it. Different from the above methods, in order to alleviate challenge posed by the complementary information excavation of feature extraction network, this paper rethinks the deep learning-based fusion idea, that is, complementary-redundant information transfer, which can effectively avoid weak feature loss of the source images, and transfer those weak details to the fusion results. Specifically, the core idea of the proposed method is shown in Fig. 1. We consider that the infrared and visible images of the same scene cover both shared and modality-specific (complementary) features. If the infrared-specific features are transferred into the visible one, we can obtain features containing shared, infrared-specific and visible-specific information, *i.e.* redundant features, and vice versa. Compared to the complementary feature based fusion, redundant feature based fusion can not only reduce the burden of feature extraction network mining complementary information, but also avoid the complementary information loss in the fusion process, getting rid of the reliance on complex fusion schemes.

Based on the above ideas, we propose a dedicated complementary-redundant information

transfer network (C-RITNet) consisting of mutual information transfer (MIT) module, structure information preserved redundant information acquisition (SIPRIA) module and fusion result reconstruction (FRR) module. MIT is composed of three parts: image inversion (II), feature extraction (FE) and mutual representation learning (MRL). II mainly facilitates the feature extraction network to obtain richer information. FE is responsible for extracting features from the input images for subsequent information transfer and fusion. MRL realizes interactive information transmission between infrared and visible source images, achieving complementary-redundant information transfer. SIPRIA contains redundant information acquisition supervised by source image (RIASSI) module and structure information preservation (SIP) module. RIASSI ensures that the complementary information after MRL can become redundant one. SIP promises that the edge structure information of the source images can be transferred to the fusion result. FRR constructs the final fusion image. The above design can effectively alleviate complementary feature extraction challenge, and meanwhile avoid designing complex fusion mechanism to aggregate complementary information. Furthermore, similar to [14], we adopt a mutual promotion training paradigm (MPTP) between two SIPRIAs and the MIT. Concretely, we divide the whole training process to two circulative phases, in other words they are trained in turn. In the first cycle phase, we train MIT to have the basic ability of information transfer by performing interactive feature representation. And then in the second cycle phase, we train two SIPRIAs to create impressive edge information for fusion, treating the fusion results obtained by MIT as “labels” to further improve the redundant feature and edge details extraction ability of two SIPRIAs. In summary, the main contributions of the proposed method are as follows:

- We reconsider the IVIF task from a new aspect, and propose an innovative idea, which transfers complementary information into redundant one to avoid the tricky complementary information extraction and aggregation problem.
- Benefited from this interesting notion, we exploit an efficient IVIF model C-RITNet to realize complementary-redundant information transfer in source infrared and visible images. Meanwhile, a feature protection mechanism is implanted, migrating detailed edge information to the fusion result.
- Extensive experiments conducted on three publicly available datasets demonstrate the effectiveness of our method, as well as show its superiority over other state-of-the-art (SOTA) models.

The rest of this article is organized as follows: Section 2 discusses typical deep learning based

and high-level task-driven IVIF methods. In Section 3, we describe the details of the proposed method. Section 4 shows the experimental results and analysis, and Section 5 summarizes the work and draws some conclusions.

## 2. Related Work

The IVIF task has been extensively explored for years and attracted much attention from the community due to its wide application prospects. In this section, we will briefly review the existing deep learning based IVIF algorithms that are closely related to ours and some high-level task-driven IVIF algorithms.

### 2.1. Deep Learning Based Infrared-Visible Image Fusion

**CNN-based methods.** In recent years, convolution neural network (CNN) dominates the field of image fusion in virtue of its strong adaptability. Commonly, the entire image fusion procedure includes feature extraction, feature fusion and image reconstruction. Some methods merely use CNN to realize activity level measurement and generate a weight map for hand-crafted features [15, 16], while the main fusion process remains traditional ways. Other methods adopt end-to-end mode, carrying out every step in image fusion with CNN. For instance, Zhang et al. [17] explored an end-to-end framework to maintain the proportion of gradient and intensity through the intensity and gradient paths. They modeled a general loss function and adjusted the hyper-parametric for different image fusion missions. In order to prompt the network to extract and merge the meaningful features purposefully, Ma et al. [18] defined desired information for infrared and visible image fusion via introducing a salient target mask. Their network can simultaneously fuse infrared and visible images and achieve salient target detection. Moreover, Xu et al. [19] trained a unified model for multi-fusion tasks with elastic weight consolidation considering the cross-fertilization between different image fusion missions. However, the fusion network cannot exhibit its full potential performance since the specificity of fusion tasks, *i.e.*, without ground-truth.

**AE-based methods.** Given that the auto-encoder (AE) structure can learn effective feature representation in an unsupervised manner, AE-based methods are utterly suitable for IVIF task since there commonly lacks fused ground-truth. Most of them trained an auto-encoder to achieve both feature extraction and image reconstruction. Typically, Li et al. [20] presented a novel deep learning architecture with encoding network combined by convolutional layers, fusion layer and dense block, while the fused image was reconstructed by decoder. Furthermore, they introduced

NestFuse [21] and RFN-Nest [22] to preserve significant amounts of information from input data in a multi-scale perspective. Specifically, the latter designed the detail preservation and feature enhancement loss functions to integrate more useful information from source images. To address the limitation that existing image fusion methods always use hand-crafted fusion rules due to the uninterpretability of deep feature maps, Xu et al. [23] proposed an unsupervised deep learning method to realize the interpretable importance evaluation of feature maps.

**GAN-based methods.** Thanks to the strong ability to estimate probability distributions, the generative adversarial network (GAN) is ideal for unsupervised tasks such as image fusion. Ma et al. [24] played an adversarial game between a generator and a discriminator for the first time, keeping the infrared thermal radiation information and preserving the visible appearance texture information. Unfortunately, a single discriminator is prone to lead the fused image to be similar to only one of the source images, causing the loss of some information. Therefore, DDcGAN [25], a dual-discriminator conditional generative adversarial network was designed to simultaneously keep the most important feature information in infrared and visible images. Besides, the existing GAN-based infrared and visible image fusion methods cannot perceive the most discriminative regions, and hence fail to highlight the typical parts existing in infrared and visible images. To this end, AttentionFGAN [26] integrated multi-scale attention mechanism into both generator and discriminator of GAN to capture more typical regions. Subsequently, GANMcC [27] was devised to transform image fusion into multi-distribution simultaneous estimation problem, which made the fused results have both the distributions of infrared and visible domains in a more balanced manner.

Nevertheless, above mentioned deep learning-based approaches put emphasis on extracting and integrating the complementary information from the infrared and visible images, which is an extremely hard problem. To this end, we rethink the IVIF task from a brand new aspect, focusing more on the redundant information excavation which is relatively easier to achieve.

## 2.2. High-level Task-Driven Infrared-Visible Image Fusion

Low-level vision tasks are often pre-processed and serve for downstream high-level vision tasks, *e.g.* object detection, semantic segmentation, *etc.*. For the infrared and visible image fusion task, Tang et al. [28] introduced the semantic loss to integrate more semantic information into fused images. They further incorporated image registration, image fusion, and semantic requirements of high-level vision tasks into a single framework and proposed a novel image registration and fusion method, named SuperFusion [29]. Consequently, since object detection

focuses on sparse object regions in images, and it plays a more important role in disaster rescue and traffic management, which is unlike semantic segmentation, Sun et al. [30] constructed a detection-driven infrared and visible fusion network that used detection-driven losses to provide task-related information for the learning of the image fusion network. More recently, Liu et al. [31] proposed a bilevel optimization formulation for the joint problem of fusion and detection, named TarDAL network for fusion and a commonly used detection network.

However, high-level vision task-driven image fusion often requires elaborately designed downstream network to tackle the high-level vision task, which is relatively cumbersome and lacking in generality. Conversely, our proposed method is more universal without specific down-stream task oriented framework design.

### 3. Proposed Method

#### 3.1. Overview

Most existing IVIF methods are dedicated to mining the complementary information in two source images, which is quite challenging. Therefore, we rethink the problem from another new perspective, where we focus on mining the redundant information in infrared and visible images, since such information is relatively easy to acquire and utilize in sequential fusion process. To be more specific, we propose a specialized complementary-redundant information transfer framework to tactfully evade the complementary information extraction problem during infrared and visible image fusion.

Pipeline of the proposed C-RITNet is shown in Fig. 2, which consists of the mutual information transfer (MIT) module, the structure information preserved redundant information acquisition (SIPRIA) module and the fusion result reconstruction (FRR) module. MIT mutually represents features from two modalities, roughly transferring complementary information into redundant one. SIPRIA aims to extract redundant as well as abundant information, especially edge structure details from source images of two modalities. Besides, it is noteworthy that we do not adopt the end-to-end training paradigm but choose multi-stage mutual promotion training strategy to achieve effective interaction and co-reinforcement between MIT and SIPRIA.

#### 3.2. Mutual information transfer

We design the mutual information transfer (MIT) module to realize complementary to redundant information transfer. MIT consists of three key components, namely image inversion

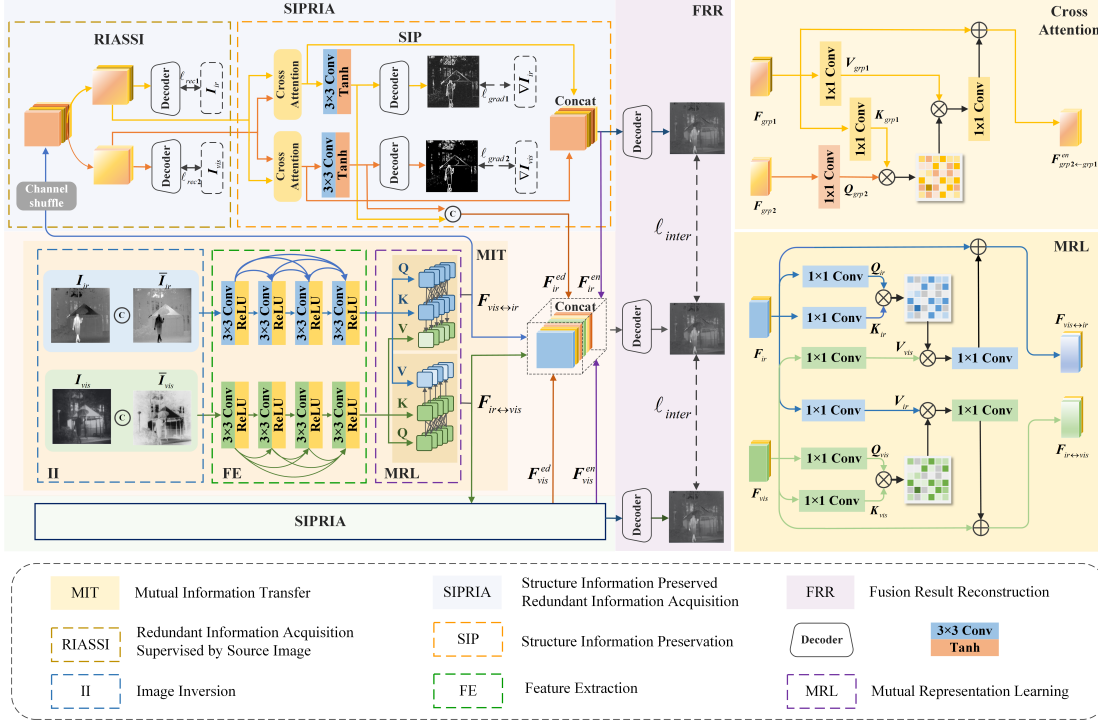


Figure 2: The overall architecture of proposed method. In phaseM, the input concatenated infrared and visible image pairs  $I'_{ir}$  and  $I'_{vis}$  are fed into the infrared-visible feature encoder  $E_{ir}$  and  $E_{vis}$  respectively to obtain features  $F_{ir}$  and  $F_{vis}$ . MIT is performed on  $F_{ir}$  and  $F_{vis}$  to achieve basic complementary-redundant information transfer, getting transferred features  $F_{vis \leftrightarrow ir}$  and  $F_{ir \leftrightarrow vis}$ . In phaseS, we then send  $F_{vis \leftrightarrow ir}$  and  $F_{ir \leftrightarrow vis}$  to SIPRIA and attain  $F_{ir}^{ed}$ ,  $F_{ir}^{en}$ ,  $F_{vis}^{ed}$ , and  $F_{vis}^{en}$ , ensuring successful information transfer and effectively preserving structure information. Finally,  $F_{vis \leftrightarrow ir}$ ,  $F_{ir}^{ed}$ ,  $F_{ir}^{en}$ ,  $F_{ir \leftrightarrow vis}$ ,  $F_{vis}^{ed}$ , and  $F_{vis}^{en}$  are concatenated together and sent to the decoder  $D_{fuse}$  to obtain the final fusion result  $I_{fused}$ .

(II), feature extraction (FE), and mutual representation learning (MRL). Below we describe the concrete structures of II, FE and MRL.

### 3.2.1. Image inversion and feature extraction

To make better use of the content in relatively over-exposed areas, literature [32] inverted the source image so that the originally over-exposed regions would appear like underexposed ones in the inverted image. We find that the salient targets in grayscale inverted image tend to resemble that in the corresponding image from another modality, *i.e.*, the salient target in inverted infrared image is alike with that in its corresponding visible image, and so does the inverted visible image. Thus, concatenating the original image and its inverted image will facilitate the complementary-redundant information transfer. Given source images  $I_{ir}$  and  $I_{vis}$ , we invert them by  $\bar{I}_{ir} = 1 - I_{ir}$  and  $\bar{I}_{vis} = 1 - I_{vis}$ . Pairs of  $I_{ir}$  and  $\bar{I}_{ir}$  are concatenated in channel dimensions to obtain  $I'_{ir}$ , and pairs of  $I_{vis}$  and  $\bar{I}_{vis}$  are concatenated to obtain  $I'_{vis}$ .  $I'_{ir}$  and  $I'_{vis}$  are fed into the infrared-visible feature encoder  $E_{ir}$  and  $E_{vis}$ , respectively. The



extracted infrared and visible image features are presented by

$$\begin{aligned}\mathbf{F}_{ir} &= \mathbf{E}_{ir}(\mathbf{I}'_{ir}), \\ \mathbf{F}_{vis} &= \mathbf{E}_{vis}(\mathbf{I}'_{vis}),\end{aligned}\tag{1}$$

where  $\mathbf{E}_{ir}$  and  $\mathbf{E}_{vis}$  have the same structure but do not share parameters, which follows the residual dense network [33].

### 3.2.2. Mutual representation learning

The architecture of MRL module is presented in Fig. 2, which strives to transfer complementary information hidden in source images to redundant one through mutual modality feature representation.

Similar to attention mechanism in Transformer [34], the infrared image feature  $\mathbf{F}_{ir} \in \mathbb{R}^{C \times H \times W}$  (where  $H$  and  $W$  are the height and width,  $C$  is the number of channels) and the visible image feature  $\mathbf{F}_{vis} \in \mathbb{R}^{C \times H \times W}$  pass through convolutions to generate Query  $\mathbf{Q}_{ir} \in \mathbb{R}^{C \times H \times W}$ , Key  $\mathbf{K}_{ir} \in \mathbb{R}^{C \times H \times W}$ , Value  $\mathbf{V}_{ir} \in \mathbb{R}^{C \times H \times W}$ , and Query  $\mathbf{Q}_{vis} \in \mathbb{R}^{C \times H \times W}$ , Key  $\mathbf{K}_{vis} \in \mathbb{R}^{C \times H \times W}$ , Value  $\mathbf{V}_{vis} \in \mathbb{R}^{C \times H \times W}$ , respectively. Given  $\mathbf{F}_{ir}$  and  $\mathbf{F}_{vis}$ , their mutual feature representations are obtained through information transfer:

$$\begin{aligned}\tilde{\mathbf{F}}_{vis \leftrightarrow ir} &= \text{softmax}\left(\frac{\mathbf{Q}_{ir}(\mathbf{K}_{ir})^T}{\sqrt{d}}\right)\mathbf{V}_{vis}, \\ \tilde{\mathbf{F}}_{ir \leftrightarrow vis} &= \text{softmax}\left(\frac{\mathbf{Q}_{vis}(\mathbf{K}_{vis})^T}{\sqrt{d}}\right)\mathbf{V}_{ir},\end{aligned}\tag{2}$$

where  $\leftrightarrow$  is cross-modality mutual representation,  $\sqrt{d}$  is a normalization factor, and  $T$  is transpose operation. To further enhance the gained interactive feature representation and avoid information loss, we perform the following operations:

$$\begin{aligned}\mathbf{F}_{vis \leftrightarrow ir} &= \text{Conv}_{1 \times 1}(\tilde{\mathbf{F}}_{vis \leftrightarrow ir}) \oplus \mathbf{F}_{ir}, \\ \mathbf{F}_{ir \leftrightarrow vis} &= \text{Conv}_{1 \times 1}(\tilde{\mathbf{F}}_{ir \leftrightarrow vis}) \oplus \mathbf{F}_{vis},\end{aligned}\tag{3}$$

where  $\text{Conv}_{1 \times 1}$  is  $1 \times 1$  convolution.  $\oplus$  denotes summing operation.

### 3.3. Structure information preserved redundant information acquisition

Infrared SIPRIA generates  $\mathbf{F}_{ir}^{en}$  and  $\mathbf{F}_{ir}^{ed}$ . Similarly, visible SIPRIA generates  $\mathbf{F}_{vis}^{en}$  and  $\mathbf{F}_{vis}^{ed}$ .  $\mathbf{F}_m^{en}$  ( $m \in ir, vis$ ) are enhanced features added to the final fusion process, avoiding information loss, while  $\mathbf{F}_m^{ed}$  are edge detail features injected to the fused results to help with

the structure information preservation. SIPRIA mainly consists of RIASSI and SIP, which will be demonstrated in detail as follows.

### 3.3.1. Redundant information acquisition supervised by source image

To further ensure the complementary-redundant information transfer after mutual representation learning, RIASSI is proposed to enable the features injected to the fusion process to have abundant information from both infrared and visible modalities by elaborately designing image reconstruction, so as to maximize the redundancy of the whole network. The specific structure of RIASSI is shown in Fig. 2.  $\mathbf{F}_{vis\leftrightarrow ir}$  and  $\mathbf{F}_{ir\leftrightarrow vis}$  are fed into infrared and visible RIASSI, respectively. Take infrared RIASSI as example, to guarantee that the complementary information is transferred to redundant one after MRL, we first shuffle all the channels of  $\mathbf{F}_{vis\leftrightarrow ir}$ , and then divide the first half of  $\mathbf{F}_{vis\leftrightarrow ir}$  by channel as  $\mathbf{F}_{grp1}$ , the rest half as  $\mathbf{F}_{grp2}$ . The images  $\hat{\mathbf{I}}_{grp2}$  and  $\hat{\mathbf{I}}_{grp1}$  are respectively reconstructed with  $\mathbf{F}_{grp1}$  and  $\mathbf{F}_{grp2}$  through decoders  $\mathbf{D}_1^{rec}$  and  $\mathbf{D}_2^{rec}$  (composed of  $3 \times 3$  convolution and  $Tanh$  activation function), whose network structures are the same but with different parameters. To encourage  $\mathbf{F}_{grp1}$  and  $\mathbf{F}_{grp2}$  to cover more modality-redundant information, the reconstruction loss is defined as:

$$\begin{aligned}\ell_{rec1} &= \|\hat{\mathbf{I}}_{grp1} - \mathbf{I}_{ir}\|_1, \\ \ell_{rec2} &= \|\hat{\mathbf{I}}_{grp2} - \mathbf{I}_{vis}\|_1, \\ \ell_{rec} &= \ell_{rec1} + \ell_{rec2}.\end{aligned}\tag{4}$$

### 3.3.2. Structure information preservation

As aforementioned, edge detail information plays an important role in the infrared and visible image fusion since it can facilitate subsequent processing and help in decision making. Therefore, we design SIP module to preserve rich edge features, whose structure is displayed in Fig. 2. Firstly, cross attention is performed on both  $\mathbf{F}_{grp1}$  and  $\mathbf{F}_{grp2}$  together to obtain interactive and enhanced features. Mathematically, the interactive enhancement process is denoted as:

$$\begin{aligned}\tilde{\mathbf{F}}_{grp2\leftarrow grp1} &= \text{softmax}\left(\frac{\mathbf{Q}_{grp2}(\mathbf{K}_{grp1})^T}{\sqrt{d}}\right)\mathbf{V}_{grp1}, \\ \tilde{\mathbf{F}}_{grp1\leftarrow grp2} &= \text{softmax}\left(\frac{\mathbf{Q}_{grp1}(\mathbf{K}_{grp2})^T}{\sqrt{d}}\right)\mathbf{V}_{grp2},\end{aligned}\tag{5}$$

where  $\leftarrow$  denotes feature interaction,  $\mathbf{Q}_{grp1}, \mathbf{Q}_{grp2} \in \mathbb{R}^{C \times H \times W}$ ,  $\mathbf{K}_{grp1}, \mathbf{K}_{grp2} \in \mathbb{R}^{C \times H \times W}$ , and  $\mathbf{V}_{grp1}, \mathbf{V}_{grp2} \in \mathbb{R}^{C \times H \times W}$  are the results of  $\mathbf{F}_{grp1}$  and  $\mathbf{F}_{grp2}$  passed through  $1 \times 1$  convolution,

respectively.  $\sqrt{d}$  is a normalization factor, and  $T$  is transpose operation. To further enhance the features, the following operations are performed:

$$\begin{aligned}\mathbf{F}_{grp2\leftarrow grp1}^{en} &= Conv_{1\times 1}(\tilde{\mathbf{F}}_{grp2\leftarrow grp1}) \oplus \mathbf{F}_{grp1}, \\ \mathbf{F}_{grp1\leftarrow grp2}^{en} &= Conv_{1\times 1}(\tilde{\mathbf{F}}_{grp1\leftarrow grp2}) \oplus \mathbf{F}_{grp2}.\end{aligned}\tag{6}$$

Secondly, we apply two encoders  $\mathbf{E}_1^{ed}$  and  $\mathbf{E}_2^{ed}$  composed of  $3 \times 3$  convolution and  $Tanh$  activation function to  $\mathbf{F}_{grp2\leftarrow grp1}^{en}$  and  $\mathbf{F}_{grp1\leftarrow grp2}^{en}$  so as to obtain edge features  $\mathbf{F}_{grp2\leftarrow grp1}^{ed}$  and  $\mathbf{F}_{grp1\leftarrow grp2}^{ed}$ , which are expected to capture more edge-related information:

$$\begin{aligned}\mathbf{F}_{grp2\leftarrow grp1}^{ed} &= \mathbf{E}_1^{ed}(\mathbf{F}_{grp2\leftarrow grp1}^{en}), \\ \mathbf{F}_{grp1\leftarrow grp2}^{ed} &= \mathbf{E}_2^{ed}(\mathbf{F}_{grp1\leftarrow grp2}^{en}).\end{aligned}\tag{7}$$

To ensure that the network can extract rich edge details,  $\mathbf{F}_{grp2\leftarrow grp1}^{ed}$  and  $\mathbf{F}_{grp1\leftarrow grp2}^{ed}$  are fed into decoders  $\mathbf{D}_1^{ed}$  and  $\mathbf{D}_2^{ed}$  (composed of  $3 \times 3$  convolution and  $Tanh$  activation function) to attain the reconstructed images  $\hat{\mathbf{I}}_1^{ed}$  and  $\hat{\mathbf{I}}_2^{ed}$ . The gradient loss is performed to force  $\mathbf{E}_1^{ed}$  and  $\mathbf{E}_2^{ed}$  to extract rich edge features:

$$\begin{aligned}\ell_{grad1} &= \|\nabla \hat{\mathbf{I}}_1^{ed} - \nabla \mathbf{I}_{ir}\|_1, \\ \ell_{grad2} &= \|\nabla \hat{\mathbf{I}}_2^{ed} - \nabla \mathbf{I}_{vis}\|_1, \\ \ell_{grad} &= \ell_{grad1} + \ell_{grad2},\end{aligned}\tag{8}$$

where  $\nabla$  denotes Laplacian gradient operator.

At this point, we can obtain the edge features extracted by SIP, which can be expressed as:

$$\mathbf{F}^{ed} = [\mathbf{F}_{grp1\leftarrow grp2}^{ed}, \mathbf{F}_{grp2\leftarrow grp1}^{ed}],\tag{9}$$

where  $[\cdot]$  denotes channel-wise concatenation. For infrared and visible SIPRIA,  $\mathbf{F}_{ir}^{ed}$  and  $\mathbf{F}_{vis}^{ed}$  denote the edge features from them, respectively.

Furthermore, since information loss is inevitable in feature extraction, we also add those enhanced features with rich information to the main fusion procedure to ensure more informative fused results. The enhanced feature in SIPRIA can be expressed as:

$$\mathbf{F}^{en} = [\mathbf{F}_{grp1\leftarrow grp2}^{en}, \mathbf{F}_{grp2\leftarrow grp1}^{en}].\tag{10}$$

$\mathbf{F}_{ir}^{en}$  and  $\mathbf{F}_{vis}^{en}$  denote the enhanced features from infrared and visible SIPRIA, respectively.

### 3.4. Fusion result reconstruction

To transfer complementary information to redundant information, we present the above MIT module to achieve mutual feature representation between two complementary modalities images, and two SIPRIAs to ease MIT of transferring information from different modalities, together for more visually pleasant fusion results. As for the fusion process, we concatenate the mutual represented features of different modalities  $\mathbf{F}_{vis\leftrightarrow ir}$  and  $\mathbf{F}_{ir\leftrightarrow vis}$  in MIT and those acquired useful redundant information from infrared and visible SIPRIA, *i.e.*,  $\mathbf{F}_{ir}^{ed}$ ,  $\mathbf{F}_{ir}^{en}$ ,  $\mathbf{F}_{vis}^{ed}$ , and  $\mathbf{F}_{vis}^{en}$ , formulated as follows:

$$\mathbf{I}_{fused} = \mathbf{D}_{fuse}([\mathbf{F}_{vis\leftrightarrow ir}, \mathbf{F}_{ir}^{ed}, \mathbf{F}_{ir}^{en}, \mathbf{F}_{ir\leftrightarrow vis}, \mathbf{F}_{vis}^{ed}, \mathbf{F}_{vis}^{en}]), \quad (11)$$

where  $\mathbf{D}_{fuse}$  stands for the decoder made up of  $3 \times 3$  convolution and *Tanh* activation.

To retain clear edge details and rich texture information in the fused image, we adopt joint gradient loss  $\ell_{JGrad}$ . The gradient of the fused image is forced to approach the maximum value between the infrared and visible image gradients.  $\ell_{JGrad}$  is formulated as:

$$\ell_{JGrad} = \|\mathbf{O}(\max(|\nabla \mathbf{I}_{ir}|, |\nabla \mathbf{I}_{vis}|)) - \nabla \mathbf{I}_{fused}\|_1, \quad (12)$$

where  $\nabla$  is Laplacian gradient operator.  $\max(\cdot)$  denotes taking the maximum value.  $\mathbf{O}(|x|) = x$  denotes finding the original gradient value before taking its absolute value.

In addition, to retain the saliency targets from the two images, we introduce the intensity loss, which can be expressed as:

$$\begin{aligned} \omega_{ir} &= \mathbf{S}_{I_{ir}} / (\mathbf{S}_{I_{ir}} - \mathbf{S}_{I_{vis}}), \omega_{vis} = 1 - \omega_{ir}, \\ \ell_{int} &= \|(\omega_{ir} \odot \mathbf{I}_{ir} + \omega_{vis} \odot \mathbf{I}_{vis}) - \mathbf{I}_{fused}\|_1, \end{aligned} \quad (13)$$

where  $\mathbf{S}_{I_{ir}}$  and  $\mathbf{S}_{I_{vis}}$  denote saliency matrices of  $\mathbf{I}_{ir}$  and  $\mathbf{I}_{vis}$ , which can be computed according to references [35, 36, 31, 37].  $\omega_{ir}$  and  $\omega_{vis}$  denote the weight maps for  $\mathbf{I}_{ir}$  and  $\mathbf{I}_{vis}$ , respectively.  $\odot$  denotes element-wise multiplying operation.

The overall reconstruction loss in MIT is computed by

$$\ell_{mit} = \ell_{int} + \lambda_{JG} \ell_{JGrad}, \quad (14)$$

where  $\lambda_{JG}$  is the hyper-parameter.

For infrared SIPRIA,  $\mathbf{F}_{ir}^{en}$  is fed into the decoder  $\mathbf{D}_{ir}^{en}$  (composed of  $3 \times 3$  convolution and  $Tanh$  activation function) to obtain reconstructed image  $\hat{\mathbf{I}}_{ir}^{sipria}$ . We use the content loss similar with Eq. (13) to ensure abundant valuable information in enhanced features:

$$\ell_{content}^{en} = \|(\boldsymbol{\omega}_{ir} \odot \mathbf{I}_{ir} + \boldsymbol{\omega}_{vis} \odot \mathbf{I}_{vis}) - \hat{\mathbf{I}}_{ir}^{sipria}\|_1. \quad (15)$$

To encourage the restoration of texture details, we model the gradient distribution and develop an edge loss similar with Eq. (12) as

$$\ell_{edge}^{en} = \|O(\max(|\nabla \mathbf{I}_{ir}|, |\nabla \mathbf{I}_{vis}|)) - \nabla \hat{\mathbf{I}}_{ir}^{sipria}\|_1. \quad (16)$$

The overall enhancement loss is

$$\ell_{en} = \ell_{content}^{en} + \lambda_{edge} \ell_{edge}^{en}, \quad (17)$$

where  $\lambda_{edge}$  is the hyper-parameter to balance the content and edge losses. To sum up, the total loss in each SIPRIA can be computed by

$$\ell_{sipria} = \ell_{rec} + \ell_{grad} + \ell_{en}. \quad (18)$$

### 3.5. Mutual Promotion Training Paradigm

Since the mutual represented features from MIT, and edge details, enhanced features from two SIPRIAs all have great influence on the final fusion results, making them collaborate with each other to achieve mutual reinforcement becomes a vital step. Simply, we divide the whole training process to two circulative phases, namely phaseM and phaseS.

In the first phaseM, we train MIT to have the basic complementary-redundant information transfer and fusion ability. In the first phaseS, two SIPRIAs are trained to create impressive supplementary information, *i.e.*  $\mathbf{F}_m^{ed}$  and  $\mathbf{F}_m^{en}$  ( $m \in \{ir, vis\}$ ), which is also the important guarantee of MIT. It is noteworthy that in the next phaseM, MIT realizes fusion based on the transferred features and injected features from two SIPRIA in the previous phaseS. In this phaseM, we fix the parameters in both two SIPRIAs which have been optimized before and train MIT. As for phaseS training, once the network in MIT get trained, we fix the optimized parameters of MIT trained in earlier phaseM, and take the fused results  $\mathbf{I}_{fused}$  as ‘‘labels’’, pulling close ‘‘labels’’ and

two enhanced redundant fusion results  $\hat{\mathbf{I}}_{ir}^{sipria}$  and  $\hat{\mathbf{I}}_{vis}^{sipria}$  through Kullback-Leibler Divergence, formulated as:

$$\ell_{inter} = \text{KL}(\mathbf{I}_{fused} || \hat{\mathbf{I}}_{ir}^{sipria}) + \text{KL}(\mathbf{I}_{fused} || \hat{\mathbf{I}}_{vis}^{sipria}). \quad (19)$$

In this way, the KL Divergence forces networks in two SIPRIAs to learn better edge details and enhanced features injected to the fusion process, getting added information with higher quality. In the next training stage of MIT, the fused results will be naturally improved with the help of better additional information consequently. By now, a virtuous mutual promotion training cycle has been formed. We further demonstrate the pseudo code of our proposed training paradigm as follows.

---

**Algorithm 1** Mutual Promotion Training Paradigm.

---

**Input:** infrared image pair  $\mathbf{I}'_{ir}$ , infrared image pair  $\mathbf{I}'_{vis}$

**Output:** fused image  $\mathbf{I}_{fused}$

Sample a batch of source data to  $\mathbf{E}_{ir}$  and  $\mathbf{E}_{vis}$ .

Initialize related encoders,  $\mathbf{Q}$ ,  $\mathbf{K}$ ,  $\mathbf{V}$  and decoders in MIT and SIPRIAs.

**for**  $iter=1, \dots, Iteration_{Maximum}$  **do**

**if**  $iter \% 200 = \text{even number (phaseM)}$  **then**

Train MIT.

Update  $\mathbf{E}_{ir}$ ,  $\mathbf{E}_{vis}$ ,  $\mathbf{Q}_{ir}$ ,  $\mathbf{K}_{ir}$ ,  $\mathbf{V}_{ir}$ ,  $\mathbf{Q}_{vis}$ ,  $\mathbf{K}_{vis}$ ,  $\mathbf{V}_{vis}$  and  $\mathbf{D}_{fuse}$  by minimizing the loss in Eq. (14).

**else**

(phaseS)

Load the learned  $\mathbf{E}_{ir}$ ,  $\mathbf{E}_{vis}$ ,  $\mathbf{Q}_{ir}$ ,  $\mathbf{K}_{ir}$ ,  $\mathbf{V}_{ir}$ ,  $\mathbf{Q}_{vis}$ ,  $\mathbf{K}_{vis}$ ,  $\mathbf{V}_{vis}$ .

Train two SIPRIAs.

Update  $\mathbf{D}_1^{rec}$ ,  $\mathbf{D}_2^{ec}$ ,  $\mathbf{Q}_{grp1}$ ,  $\mathbf{K}_{grp1}$ ,  $\mathbf{V}_{grp1}$ ,  $\mathbf{Q}_{grp2}$ ,  $\mathbf{K}_{grp2}$ ,  $\mathbf{V}_{grp2}$ ,  $\mathbf{E}_1^{ed}$ ,  $\mathbf{E}_2^{ed}$ ,  $\mathbf{D}_1^{ed}$ ,  $\mathbf{D}_2^{ed}$  and  $\mathbf{D}_{ir}^{en}$  ( $\mathbf{D}_{vis}^{en}$ ) by minimizing the loss in Eq. (18) and Eq. (19).

**end**

**end for**

---

## 4. Experiments

### 4.1. Experimental configurations

**Training dataset:** We select 148 image pairs from the RoadScene [19] benchmark as the training set in this paper, containing rich scenes, such as roads, vehicles, and pedestrians. Since such data scale is insufficient to train a network with superior performance, to expand this dataset, we randomly crop the training samples into  $120 \times 120$  patches.

**Testing dataset:** Firstly, we conduct qualitative and quantitative experiments on chosen 38 pairs of testing set from the RoadScene. Moreover, as is known to all that the generalization

ability of the deep learning-based method is also a vital indicator to evaluate model performance, we carry out the generalization experiments on 40 image pairs of the TNO [38] and the VOT2020-RGBT [39] datasets and 40 image pairs of the OTCBVS [40] dataset including scenes of busy pathway intersections on the Ohio State University campus to verify the effectiveness and generalization ability of our C-RITNet. TNO dataset contains multi-spectral nighttime imagery of various military-relevant scenarios in grayscale. VOT2020-RGBT is a RGB-infrared paired dataset involving loads of video sequences for Visual-Object-Tracking Challenge.

**Evaluation metrics:** For quantitative evaluation, six statistical metrics are selected to objectively assess the fusion performance, including correlation coefficient (CC) [41], entropy (EN) [42],  $Q^{AB/F}$  [43],  $Q^{CV}$  [44], the sum of correlations of differences (SCD) [45], and structural similarity (SSIM) [46]. CC measures the degree of linear correlation between the fused image and source images. EN evaluates the amount of information contained in the fused image from the perspective of the information theory.  $Q^{AB/F}$  measures the amount of edge information that is transferred from source images to the fused image and is based on the assumption that the edge information in the source images is preserved in the fused image.  $Q^{CV}$  is based on the human visual system model, using the Sobel operator to extract the edge information of the source images and the fusion result to obtain the edge intensity map  $G$ . Smaller  $Q^{CV}$  implies more in line with human visual perception. SCD reflects the level of correlation between information transmitted to the fused image and corresponding source images. SSIM models image loss and distortion. Moreover, a fusion algorithm with larger CC, EN,  $Q^{AB/F}$ , SCD, and SSIM indicates better fusion performance.

#### 4.2. Implementation details

We train our proposed C-RITNet on selected 148 image pairs with data augmentation from the RoadScene dataset. Since our method is a circulative two-stage model, we train each phase with batch size set to 8 and patch size set to  $120 \times 120$ .  $Iteration_{Maximum}$  is set to 1000. Furthermore, four Adam optimizers [47] ( $\beta_1 = 0.9$ , and  $\beta_2 = 0.999$ ) responsible for two SIPRIAs and two different MIT stages with initial learning rate of 0.001, which decreases to  $10^{-4}$  after 100 epochs and then to  $10^{-7}$  after 400 epochs, except for the second MIT phase with initial learning rate of  $10^{-5}$  and the same decay rate, are used to optimize two cyclical training phases under the guidance of the interaction loss  $\ell_{inter}$ . In addition, two hyperparameters  $\lambda_{edge}$  and  $\lambda_{JG}$  are set to 20. Our framework is implemented in PyTorch. All experiments are conducted on an Nvidia 3090 GPU.

Table 1: Quantitative evaluation results of ablation study on 40 pairs of infrared and visible images from TNO-VOT dataset.

Configuration	CC	EN	$Q^{AB/F}$	$Q^{CV}$	SCD	SSIM
w/o MIT	0.6874	6.7817	0.4520	598.0829	1.2261	1.3919
w/o SIPRIA	0.6843	6.9485	0.4570	524.1034	1.3557	1.3945
w/o MPTP	0.6813	7.0756	0.4143	454.8244	1.3168	1.4202
Ours	<b>0.6991</b>	<b>7.2819</b>	<b>0.5503</b>	<b>427.2510</b>	<b>1.4893</b>	<b>1.4443</b>

Please note that we simply convert source images in RoadScene, VOT2020-RGBT and OTCBVS datasets to gray to achieve fusion.

### 4.3. Ablation studies

In the above description, we mainly devise two important modules named MIT and SIPRIA to achieve complementary-redundant information transfer and edge detail preservation. In this section, we give more results under different settings on the framework and training strategy on TNO-VOT dataset, to verify the rationality of our design.

#### 4.3.1. Mutual information transfer analysis

To skillfully achieve IVIF fusion without direct complementary information excavation, we devise the complementary-redundant information transfer to concentrate more on redundant information. Specifically, we design the MIT module to achieve information transfer, as well as two SIPRIAs to help MIT ensure successful transfer process. After we change the whole network into a single feature extraction and fusion one, *i.e.*, features extracted are modality-specific, the quality of fused image declines slightly. As shown in Fig. 3(c), some edge details of the bush and handrail in the infrared image are lost, and the image contrast decreases. Furthermore, so as to demonstrate the effectiveness of the MIT more intuitively, we display the averaged infrared and visible feature maps on channel before and after the MIT module, *i.e.*,  $\mathbf{F}_{ir}$ ,  $\mathbf{F}_{vis\leftrightarrow ir}$ ,  $\mathbf{F}_{vis}$  and  $\mathbf{F}_{ir\leftrightarrow vis}$  in Fig. 4. We can clearly see that the strip on the road sign in visible image successfully transfers to the infrared image. Moreover, the wire netting and walking man in the infrared image successfully transfer to the visible image, which implies successful complementary-redundant information transfer. Besides, the quantitative results in Table 1 drop the most in practically all evaluation metrics, which speaks volumes for our complementary-redundant information transfer idea.

#### 4.3.2. Structure information preserved redundant information acquisition analysis

Two SIPRIAs are responsible for the retention and boost of edge and texture, in which RIASSI and SIP modules are also the key points in our overall framework since they can effec-



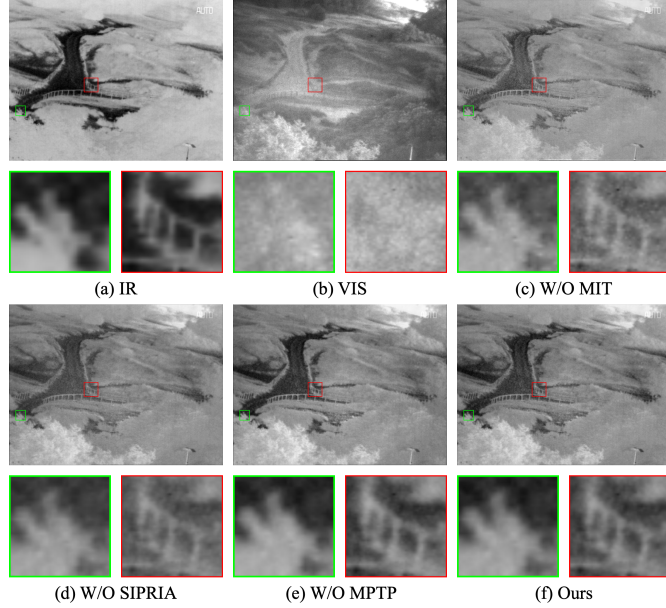


Figure 3: Vision quality comparison of the ablation study on important idea and modules. From left to right, infrared image, visible image, and the results of W/O MIT, SIPRIA, MPTP, and our C-RITNet.

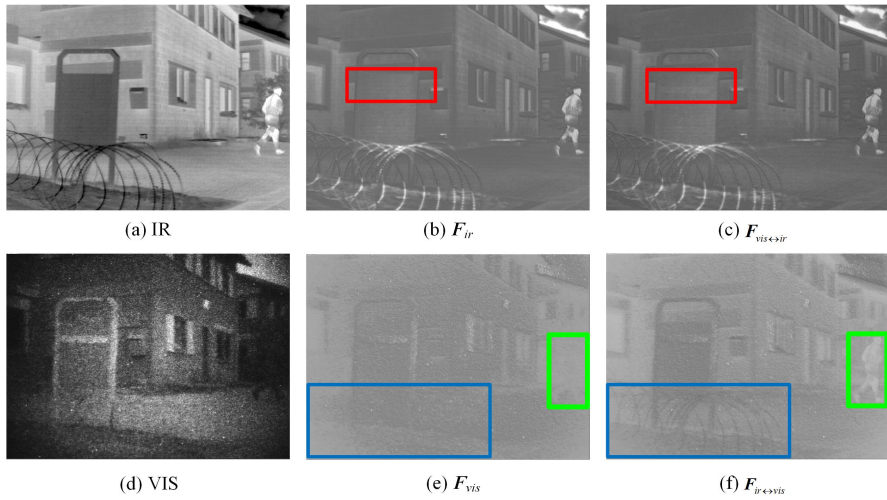


Figure 4: Infrared and visible feature maps before and after mutual information transfer.

tively enhance the edge and texture details in the fused images. When we remove both of the two SIPRIAs, the edges of nearly all the objects are indistinguishable, meanwhile the texture details blur, as shown in Fig. 3(d). On the contrary, our fusion result presents more detailed textures as shown in Fig. 3(f). Since  $Q^{AB/F}$  measures the amount of edge information that is transferred from source images to the fused image, lower  $Q^{AB/F}$  in model without SIPRIAs further indicates the effectiveness of the proposed SIPRIA module.

### 4.3.3. Mutual promotion training paradigm analysis

We propose a circulative mutual promotion training strategy to improve the final fusion performance across the board. In the ablation experiment, we adopt end-to-end training paradigm, which is to say, we train two SIPRIAs and MIT together as a whole. The visualized result is presented in Fig. 3(e). Though the visualized result is similar to ours, the quantitative results in Table 1 deteriorate. Therefore, we can conclude that MPTP provides a more effective training for the subsequent fusion.

### 4.4. Comparative experiment

To illustrate the superiority of the proposed method, we conduct comprehensive comparative experiments of fusion performance with seven SOTA competitors including RFN-Nest [22], SuperFusion [29], FusionGAN [24], U2Fusion [19], SDDGAN [48], MetaFusion[49], and LRRNet [50] on 38 image pairs of RoadScene, 40 image pairs of the TNO and the VOT2020-RGBT, and 40 image pairs of OTCBVS datasets.

#### 4.4.1. Experiments on RoadScene dataset

So as to visually observe the fusion performance of different algorithms on RoadScene dataset, we select two pairs of infrared and visible images (named #FLIR\_00288 and #FLIR\_08835, respectively), which are shown in Fig. 5. As illustrated in the green and red boxes in the #FLIR\_00288 image, our proposed C-RITNet keeps the clearest cloud edge while maintaining favourable shrub textures. RFN-Nest, FusionGAN and SDDGAN have vague overall scenes, which declines the visual effects. SuperFusion and LRRNet lose cloud information, and are unable to present satisfying contrast.

As shown in the green box of the #FLIR\_08835 image, fusion results of RFN-Nest, FusionGAN, SDDGAN, and LRRNet are relatively blurred, missing quite a lot of scene information. Although SuperFusion and U2Fusion have more sharpened pedestrain edges, the railing textures are lost, as zoomed in the red boxes. On the contrary, our fusion results obtain both clear target edges and rich texture details.

We conduct quantitative comparisons on 38 image pairs from RoadScene dataset to verify the effectiveness of our method, which is presented in Fig. 6 and Table 2. It can be seen that our method ranks first in four metrics and second in the  $Q^{CV}$  metric. The best CC, SCD and SSIM metrics demonstrate that our results contain more realistic information. The presence of the SIP module allows the  $Q^{AB/F}$  metric of our method to outperform other SOTA methods.

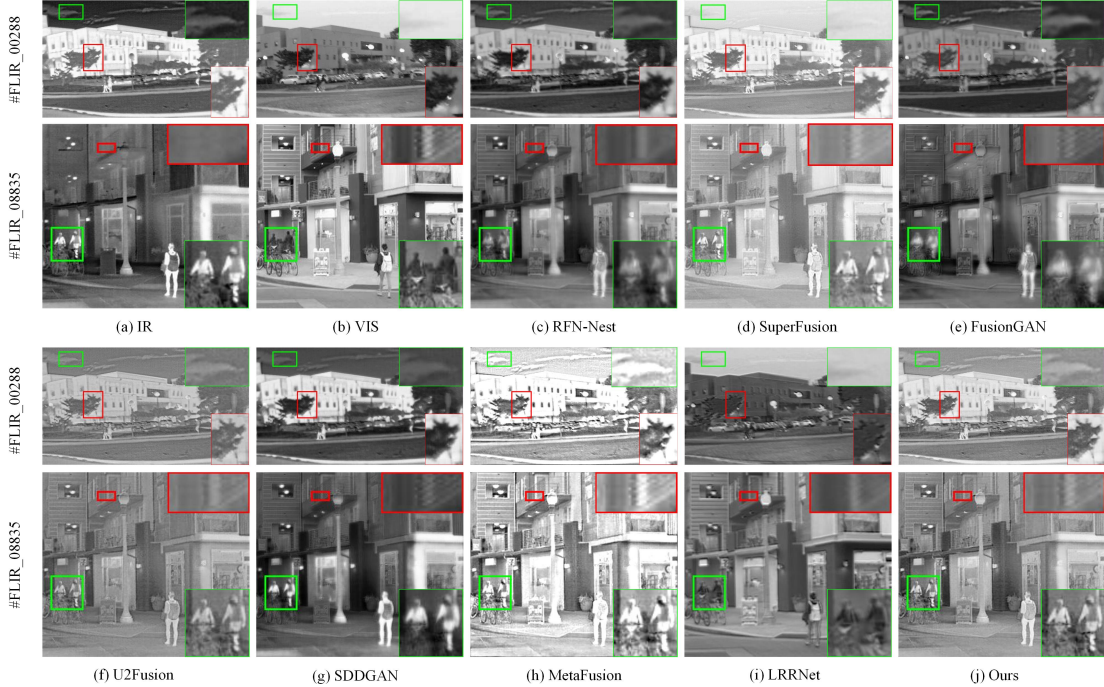


Figure 5: Vision quality comparison of our method with seven SOTA fusion methods on #FLIR\_00288 and #FLIR\_08835 images from the RoadScene dataset.

Table 2: Quantitative results of seven SOTA methods and ours on 38 image pairs from RoadScene [19] dataset. Bold: best. Italic: second best.

Methods	CC	EN	$Q^{AB/F}$	$Q^{CV}$	SCD	SSIM
RFN-Nest[22]	0.5926	<i>7.9512</i>	0.2983	1275.9437	1.2189	1.2337
SuperFusion[29]	<i>0.6719</i>	7.0620	0.4604	<b>491.2926</b>	1.3930	1.3072
FusionGAN[24]	0.5540	7.1681	0.2588	1442.2847	0.8642	1.1566
U2Fusion[19]	0.5847	6.8581	<i>0.4658</i>	1071.4871	1.1965	<i>1.3822</i>
SDDGAN[48]	0.5601	<b>7.4797</b>	0.3273	1319.1305	1.2830	1.1960
MetaFusion[49]	0.6533	7.0634	0.3441	1123.0795	<i>1.4954</i>	1.0712
LRRNet[50]	0.5558	6.9726	0.1890	1298.3829	0.5990	0.8598
Ours	<b>0.6786</b>	7.1010	<b>0.4733</b>	<i>867.5416</i>	<b>1.5388</b>	<b>1.3944</b>

Our method trails SuperFusion by a narrow margin in the  $Q^{CV}$  metric, but our fusion result preserves more detailed textures and the scene is clearer than that of other methods.

In conclusion, our C-RITNet is fully capable of excavating edge and texture features and integrating them into fused images with the help of two SIPRIA and MIT. Thereby, our method is superior to other SOTA approaches and obtains high-quality fused images.

#### 4.4.2. Experiments on TNO-VOT dataset

In order to visually observe the fusion performance of different algorithms on the selected TNO-VOT dataset, we select eight pairs of infrared and visible images. The visualized results are presented in Fig. 7. As shown in the first column of Fig. 7, nearly all methods have blurred

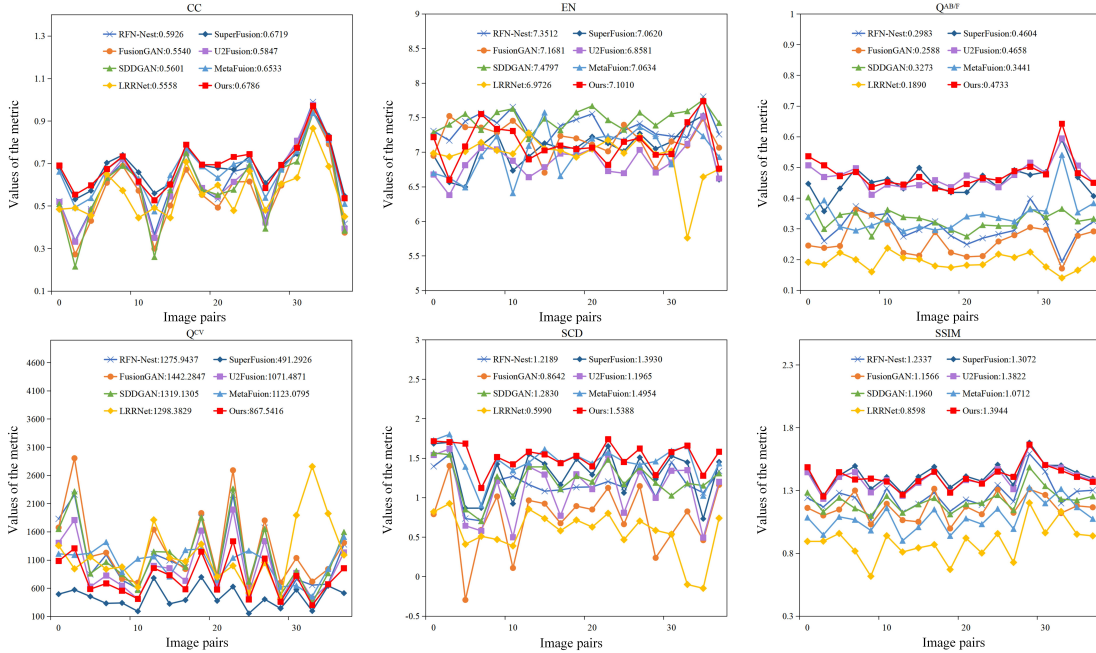


Figure 6: Quantitative results of six metrics, *i.e.*, CC, EN,  $Q^{AB/F}$ ,  $Q^{CV}$ , SCD, and SSIM, on 38 image pairs from RoadScene dataset. Seven SOTA methods are used for comparison.

wire netting edges while our method keeps clear edge information, better viewed in the zoomed-in red box. Although SuperFusion performs well in retaining texture details of the wires, it loses clouds textures in the sky, best viewed in the green box. The same situation also happens to the fourth and seventh columns of Fig. 7. On the other hand, our method preserves both edge details and background textures to the most extent.

As depicted in the second and third columns of Fig. 7, the highlighted area in the red box indicates that our proposed method could reach the sharpest edges and maintain satisfying brick textures. Moreover, in the sixth column of Fig. 7, fusion results of SuperFusion and LRRNet submerge fence into fuzzy background. Although RFN-Nest, FusionGAN, and SDDGAN have relatively clearer edges, they are still indistinct. On the contrary, our method reserves sharpened fence edges as well as considerable texture details.

Finally, as presented in the eighth column of Fig. 7, edge details of the saliency target blur in FusionGAN results, largely due to the insufficient capacity in fully modelling the data distributions of source images. Typically, fused results in U2Fusion method lose the thermal target information and cannot attract human attention. Furthermore, existing approaches tend to extract background detail features from the visible image, while acquire salient features from the infrared image. They neglect texture information in the infrared image, resulting



Figure 7: Vision quality comparison of our method with seven SOTA fusion methods on eight images from the TNO-VOT dataset. Each column represents a scene.

partly detail missing. Instead, our proposed method is able to highlight prominent target while preserving favorable contrast and edge details, as well as introducing less noise.

In conclusion, our method could retain the intensity distribution of the infrared target with more sharpened edges and skillfully exclude useless information, *i.e.* noises in visible images. We attribute this advantage to the fact that our method injects useful edge detail features into the fusion process and spontaneously exploits valuable features in source images.

The comparative results are presented in Table 3. It can be seen that our method ranks first in four metrics and second in the  $CC$  and  $Q^{CV}$  metrics. The best EN, SCD and SSIM metrics indicate that our results are the most similar with the source images, preserving the original information to the utmost extent and more natural. The idea of complementary-redundant information transfer promises the advantage of our approach over the SOTA methods. Moreover,

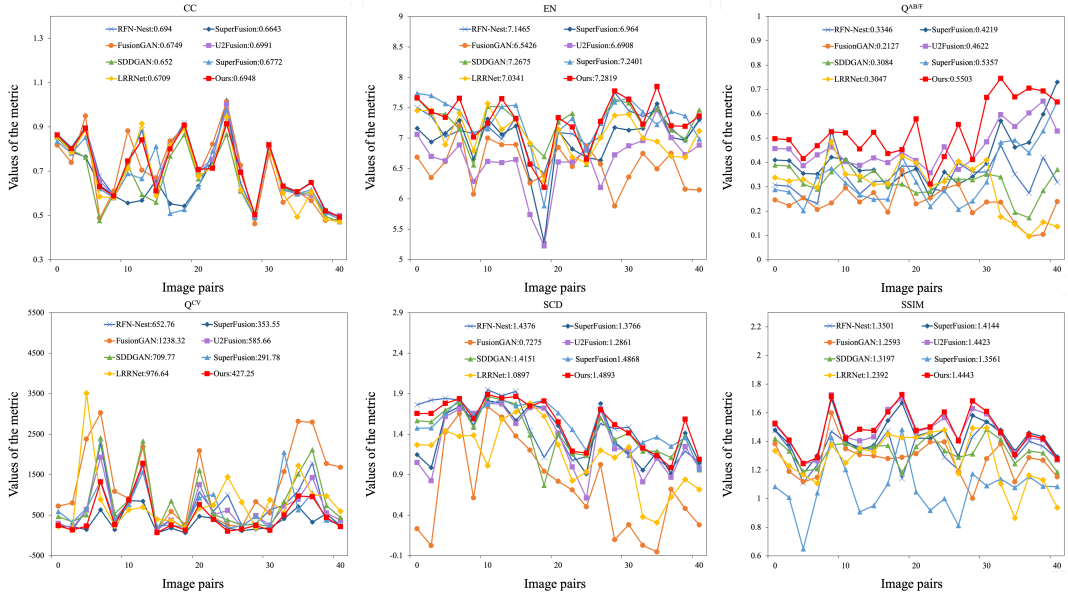


Figure 8: Quantitative results of six metrics, *i.e.*, CC, EN,  $Q^{AB/F}$ ,  $Q^{CV}$ , SCD, and SSIM, on 40 image pairs from TNO-VOT dataset. Seven SOTA methods are used for comparison.

Table 3: Quantitative results of seven SOTA methods and ours on 40 image pairs from TNO [38] and VOT [39] datasets. Bold: best. Italic: second best.

Methods	CC	EN	$Q^{AB/F}$	$Q^{CV}$	SCD	SSIM
RFN-Nest[22]	0.6989	7.1465	0.3346	652.7590	<i>1.4376</i>	1.3501
SuperFusion[29]	0.6643	6.9682	0.4081	<b>353.5487</b>	1.3611	1.4144
FusionGAN[24]	0.6790	6.5426	0.2127	1238.3200	0.7275	1.2593
U2Fusion[19]	<b>0.7032</b>	6.6908	0.4622	585.6560	1.2861	<i>1.4423</i>
SDDGAN[48]	0.6548	<i>7.2675</i>	0.3084	709.7720	1.4151	1.3197
MetaFusion[49]	0.6553	7.1829	<i>0.5434</i>	881.5672	1.2508	1.2812
LRRNet[50]	0.6749	7.0341	0.3047	976.6410	1.0897	1.2392
Ours	<i>0.6991</i>	<b>7.2819</b>	<b>0.5503</b>	<i>427.2510</i>	<b>1.4893</b>	<b>1.4443</b>

our method also performs well in  $Q^{AB/F}$ , showing that our fusion results have richer texture details and more salient targets, with the help of SIP module. Besides, C-RITNet has an excellent performance on the  $Q^{CV}$  metric only following SeAFusion, revealing that our fused images are also consistent with the human visual system. More intuitive results comparison is shown in Fig. 8.

#### 4.4.3. Experiments on OTCBVS dataset

Qualitative comparison results on OTCBVS dataset are shown in Fig. 9 to testify the generalization ability of our C-RITNet. Our method is able to provide more sharpened target edges and detailed textures. As shown in the green box of scene #video\_0001, edge and texture of the walking man with suit is much clearer in our method while other competitors blur to some extent. What’s more, though U2Fusion performs neck and neck with ours, it fails to retain the

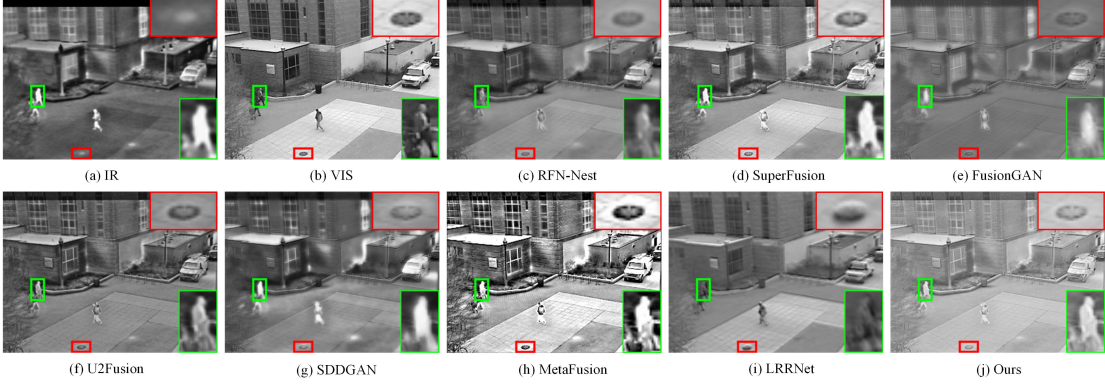


Figure 9: Vision quality comparison of our method with seven SOTA fusion methods on #video\_0001 from the OTCBVS dataset.

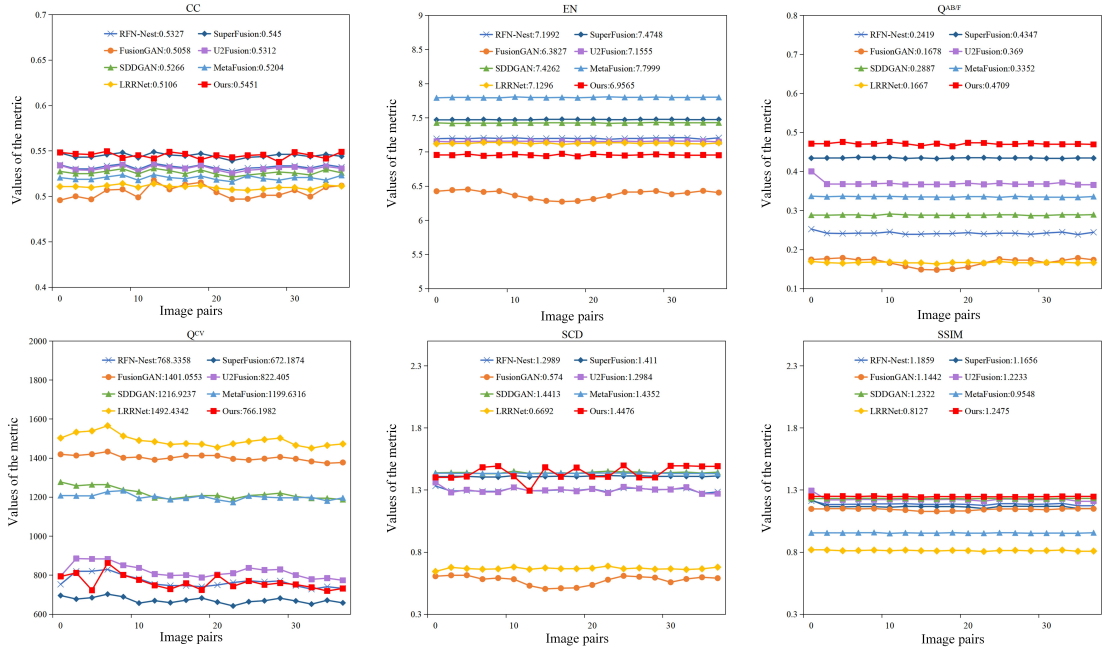


Figure 10: Quantitative results of six metrics, *i.e.*, CC, EN,  $Q^{AB/F}$ ,  $Q^{CV}$ , SCD, and SSIM, on 40 image pairs from OTCBVS dataset. Seven SOTA methods are used for comparison.

exact shape of the manhole cover, best viewed in the red zoomed-in boxes.

Table 4 gives quantitatively comparable results, and our C-RITNet has three indexes ranking first. The best CC,  $Q^{AB/F}$ , SCD and SSIM metrics imply that our results reserve the most information of the source images and have desirable texture details and salient targets. Besides, the second best in  $Q^{CV}$  metric indicates that our fusion results are more natural and human visual-friendly. More intuitively comparable results are shown in Fig. 10.

To sum up, the proposed C-RITNet is adept at transferring complementary information to redundant one, excavating useful information in source images and integrating it into fused

Table 4: Quantitative results of seven SOTA methods and ours on 40 image pairs from OTCBVS [40] dataset. Bold: best. Italic: second best.

Methods	CC	EN	$Q^{AB/F}$	$Q^{CV}$	SCD	SSIM
RFN-Nest[22]	0.5327	7.1992	0.2419	768.3358	1.2989	1.1859
SuperFusion[29]	<i>0.5450</i>	<i>7.4748</i>	<i>0.4347</i>	<b>672.1874</b>	1.4110	1.1656
FusionGAN[24]	0.5058	6.3827	0.1678	1401.0553	0.5740	1.1442
U2Fusion[19]	0.5312	7.1555	0.3690	822.4050	1.2984	1.2233
SDDGAN[48]	0.5266	7.4262	0.2887	1216.9237	<i>1.4413</i>	<i>1.2322</i>
MetaFusion[49]	0.5204	<b>7.7999</b>	0.3352	1199.6316	1.4352	0.9548
LRRNet[50]	0.5106	7.1296	0.1667	1492.4342	0.6692	0.8127
Ours	<b>0.5451</b>	6.9565	<b>0.4709</b>	<i>766.1982</i>	<b>1.4476</b>	<b>1.2475</b>

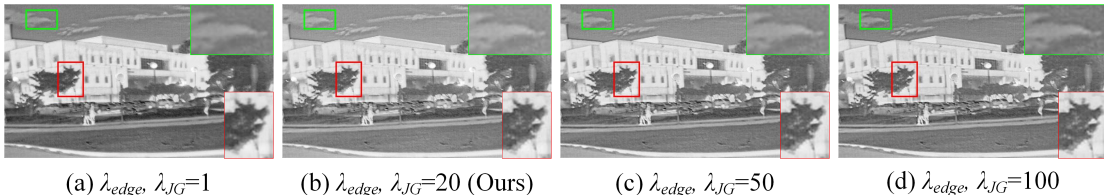


Figure 11: The fusion results with different  $\lambda_{edge}$  and  $\lambda_{JG}$ .

Table 5: Effect of different hyperparameters settings on fusion performance.

$\lambda_{edge}, \lambda_{JG}$	CC	EN	$Q^{AB/F}$	$Q^{CV}$	SCD	SSIM
1	0.6335	<b>7.3042</b>	0.4802	878.0353	1.2989	1.4926
20	<b>0.6786</b>	7.1010	<b>0.4904</b>	<b>867.5416</b>	<b>1.5388</b>	<b>1.3944</b>
50	0.6181	7.0921	0.1678	932.8368	0.5740	1.4254
100	0.6006	7.0501	0.4911	987.6895	1.2984	1.3956

images with the help of edge details and enhanced features injection from two SIPRIA in a co-reinforcement manner. Hence, our method has more advantages than other SOTA methods and attains high-quality fusion results.

#### 4.5. Analysis of hyperparameters

We perform hyperparameter analysis on RoadScene dataset [19] to validate the rationality of our C-RITNet. As described in SIP module of Section 3.3.2 and the fusion result reconstruction process in Section 3.4,  $\lambda_{edge}$  and  $\lambda_{JG}$  are the parameters controlling the degree of edge loss in the image reconstruction procedure. According to Eq. (17) and Eq. (14), the larger  $\lambda_{edge}$  and  $\lambda_{JG}$  values pay more attention to the edge maintenance. Since the loss functions for both fused image reconstruction of  $\hat{I}_{ir}^{sipria}$  ( $\hat{I}_{vis}^{sipria}$ ) and  $I_{fused}$  are the same, we change those two hyperparameters simultaneously. Now that the edge and texture details directly affect the qualities of fusion results, we assign a large value to  $\lambda_{edge}$  and  $\lambda_{JG}$ . In order to analyze the sensitivity of this parameter,  $\lambda_{edge}$  and  $\lambda_{JG}$  are set as 1, 20, 50, and 100, respectively. Vision and numerical quality results are shown in Fig. 11 and Table 5. It can be seen that when  $\lambda_{edge}$  and  $\lambda_{JG}$  are set as 20, our fusion result achieves great visual perception and quantitative best.



## 5. Conclusion

In this paper, we rethink the IVIF task from a brand new angle, focusing more on the easily acquired redundant information rather than struggling and striving on the complementary information extraction. We propose a novel mutual promoted infrared and visible image fusion algorithm with mutual information transfer and structure information preserved redundant information acquisition, which achieves effective image fusion with more texture retention. Specifically, MIT fulfills the core idea of complementary-redundant information transfer, RI-ASSI is designed to ensure that the complementary information is successfully transferred to redundant one while SIP is for structure information preservation and enhanced feature injection to avoid vital weak information loss of source images. Then, we employ interaction fusion with the help of added edge details and enhanced features to attain high-quality fused results. Given that components in previous end-to-end training strategies fail to progressively learn from one another, we adopt a mutual promotion training paradigm for better cooperation between each modules. Qualitative and quantitative comparisons with the state-of-the-arts approaches validate the superiority of our method, including edge details, texture information, and visual perception.

## Acknowledgments

This work was supported by the National Natural Science Foundation of China (Grant No.62161015).

## References

- [1] H. Zhang, H. Xu, X. Tian, J. Jiang, J. Ma, Image fusion meets deep learning: A survey and perspective, *Information Fusion* 76 (2021) 323–336.
- [2] J. Chen, X. Li, L. Luo, X. Mei, J. Ma, Infrared and visible image fusion based on target-enhanced multiscale transform decomposition, *Information Sciences* 508 (2020) 64–78.
- [3] H. Li, H. Qiu, Z. Yu, Y. Zhang, Infrared and visible image fusion scheme based on nsct and low-level visual features, *Infrared Physics & Technology* 76 (2016) 174–184.
- [4] H. Li, B. Manjunath, S. K. Mitra, Multisensor image fusion using the wavelet transform, *Graphical Models and Image Processing* 57 (3) (1995) 235–245.

- [5] X. Yan, H. Qin, J. Li, H. Zhou, J.-g. Zong, Infrared and visible image fusion with spectral graph wavelet transform, *JOSA A* 32 (9) (2015) 1643–1652.
- [6] H. Li, X. He, D. Tao, Y. Tang, R. Wang, Joint medical image fusion, denoising and enhancement via discriminative low-rank sparse dictionaries learning, *Pattern Recognition* 79 (2018) 130–146.
- [7] M. Xie, J. Wang, Y. Zhang, A unified framework for damaged image fusion and completion based on low-rank and sparse decomposition, *Signal Processing: Image Communication* 29 (2021) 116400.
- [8] Y. Zhang, M. Yang, NanLi, Z. Yu, Analysis-synthesis dictionary pair learning and patch saliency measure for image fusion, *Signal Processing* 167 (2020) 107327.
- [9] H. Li, Y. Wang, Z. Yang, R. Wang, X. Li, D. Tao, Discriminative dictionary learning-based multiple component decomposition for detail-preserving noisy image fusion, *IEEE Transactions on Instrumentation and Measurement* 69 (4) (2019) 1082–1102.
- [10] W. Xiao, Y. Zhang, H. Wang, F. Li, H. Jin, Heterogeneous knowledge distillation for simultaneous infrared-visible image fusion and super-resolution, *IEEE Transactions on Instrumentation and Measurement* 71 (2022) 5004015.
- [11] J. Ma, L. Tang, F. Fan, J. Huang, X. Mei, Y. Ma, Swinfusion: Cross-domain long-range learning for general image fusion via swin transformer, *IEEE/CAA Journal of Automatica Sinica* 9 (7) (2022) 1200–1217.
- [12] H. Li, J. Zhao, J. Li, Z. Yu, G. Lu, Feature dynamic alignment and refinement for infrared-visible image fusion: Translation robust fusion, *Information Fusion* 95 (2023) 26–41.
- [13] H. Li, Y. Cen, Y. Liu, X. Chen, Z. Yu, Different input resolutions and arbitrary output resolution: A meta learning-based deep framework for infrared and visible image fusion, *IEEE Transactions on Image Processing* 30 (2021) 4070–4083.
- [14] H. Tang, C. Yuan, Z. Li, J. Tang, Learning attention-guided pyramidal features for few-shot fine-grained recognition, *Pattern Recognition* 130 (2022) 108792.
- [15] H. Li, X. Wu, J. Kittler, Infrared and visible image fusion using a deep learning framework, in: *24th International Conference on Pattern Recognition, IEEE, 2018*, pp. 2705–2710.

- [16] Y. Liu, X. Chen, J. Cheng, H. Peng, A medical image fusion method based on convolutional neural networks, in: 20th International Conference on Information Fusion, IEEE, 2017, pp. 1–7.
- [17] H. Zhang, H. Xu, Y. Xiao, X. Guo, J. Ma, Rethinking the image fusion: A fast unified image fusion network based on proportional maintenance of gradient and intensity, in: Proceedings of the AAAI Conference on Artificial Intelligence, Vol. 34, 2020, pp. 12797–12804.
- [18] J. Ma, L. Tang, M. Xu, H. Zhang, G. Xiao, Stdfusionnet: An infrared and visible image fusion network based on salient target detection, IEEE Transactions on Instrumentation and Measurement 70 (2021) 1–13.
- [19] H. Xu, J. Ma, J. Jiang, X. Guo, H. Ling, U2fusion: A unified unsupervised image fusion network, IEEE Transactions on Pattern Analysis and Machine Intelligence 44 (1) (2020) 502–518.
- [20] H. Li, X.-J. Wu, Densefuse: A fusion approach to infrared and visible images, IEEE Transactions on Image Processing 28 (5) (2018) 2614–2623.
- [21] H. Li, X.-J. Wu, T. Durrani, Nestfuse: An infrared and visible image fusion architecture based on nest connection and spatial/channel attention models, IEEE Transactions on Instrumentation and Measurement 69 (12) (2020) 9645–9656.
- [22] H. Li, X.-J. Wu, J. Kittler, Rfn-nest: An end-to-end residual fusion network for infrared and visible images, Information Fusion 73 (2021) 72–86.
- [23] H. Xu, H. Zhang, J. Ma, Classification saliency-based rule for visible and infrared image fusion, IEEE Transactions on Computational Imaging 7 (2021) 824–836.
- [24] J. Ma, W. Yu, P. Liang, C. Li, J. Jiang, Fusiongan: A generative adversarial network for infrared and visible image fusion, Information fusion 48 (2019) 11–26.
- [25] J. Ma, H. Xu, J. Jiang, X. Mei, X.-P. Zhang, Ddcgan: A dual-discriminator conditional generative adversarial network for multi-resolution image fusion, IEEE Transactions on Image Processing 29 (2020) 4980–4995.
- [26] J. Li, H. Huo, C. Li, R. Wang, Q. Feng, Attentionfgan: Infrared and visible image fusion using attention-based generative adversarial networks, IEEE Transactions on Multimedia 23 (2020) 1383–1396.

- [27] J. Ma, H. Zhang, Z. Shao, P. Liang, H. Xu, Ganmcc: A generative adversarial network with multiclassification constraints for infrared and visible image fusion, *IEEE Transactions on Instrumentation and Measurement* 70 (2021) 1–14.
- [28] L. Tang, J. Yuan, J. Ma, Image fusion in the loop of high-level vision tasks: A semantic-aware real-time infrared and visible image fusion network, *Information Fusion* 82 (2022) 28–42.
- [29] L. Tang, Y. Deng, Y. Ma, J. Huang, J. Ma, Superfusion: A versatile image registration and fusion network with semantic awareness, *IEEE/CAA Journal of Automatica Sinica* 9 (12) (2022) 2121–2137.
- [30] Y. Sun, B. Cao, P. Zhu, Q. Hu, Defusion: A detection-driven infrared and visible image fusion network, in: *Proceedings of the 30th ACM International Conference on Multimedia, 2022*, pp. 4003–4011.
- [31] J. Liu, X. Fan, Z. Huang, G. Wu, R. Liu, W. Zhong, Z. Luo, Target-aware dual adversarial learning and a multi-scenario multi-modality benchmark to fuse infrared and visible for object detection, in: *Proceedings of the IEEE/CVF Conference on Computer Vision and Pattern Recognition, 2022*, pp. 5802–5811.
- [32] D. Han, L. Li, X. Guo, J. Ma, Multi-exposure image fusion via deep perceptual enhancement, *Information Fusion* 79 (2022) 248–262.
- [33] Y. Zhang, Y. Tian, Y. Kong, B. Zhong, Y. Fu, Residual dense network for image restoration, *IEEE Transactions on Pattern Analysis and Machine Intelligence* 43 (7) (2020) 2480–2495.
- [34] A. Vaswani, N. Shazeer, N. Parmar, J. Uszkoreit, L. Jones, A. N. Gomez, L. Kaiser, I. Polosukhin, Attention is all you need, *Advances in Neural Information Processing Systems* 30 (2017).
- [35] S. Ghosh, R. G. Gavaskar, K. N. Chaudhury, Saliency guided image detail enhancement, in: *2019 National Conference on Communications, IEEE, 2019*, pp. 1–6.
- [36] J. Liu, Y. Wu, Z. Huang, R. Liu, X. Fan, Smoa: Searching a modality-oriented architecture for infrared and visible image fusion, *IEEE Signal Processing Letters* 28 (2021) 1818–1822.
- [37] D. Wang, J. Liu, X. Fan, R. Liu, Unsupervised misaligned infrared and visible image fusion via cross-modality image generation and registration, in: *Proceedings of the Thirty-First International Joint Conference on Artificial Intelligence, 2022*, pp. 3508–3515.

- [38] A. Toet, TNO Image Fusion Dataset (10 2022). doi:10.6084/m9.figshare.1008029.v2. URL [https://figshare.com/articles/dataset/TNO\\_Image\\_Fusion\\_Dataset/1008029](https://figshare.com/articles/dataset/TNO_Image_Fusion_Dataset/1008029)
- [39] M. Kristan, A. Leonardis, J. Matas, M. Felsberg, R. Pflugfelder, J.-K. Kämäräinen, M. Danelljan, L. Č. Zajc, A. Lukežič, O. Drbohlav, et al., The eighth visual object tracking vot2020 challenge results, in: *Computer Vision–ECCV 2020 Workshops: Glasgow, UK, August 23–28, 2020, Proceedings, Part V 16*, Springer, 2020, pp. 547–601.
- [40] J. W. Davis, V. Sharma, Background-subtraction using contour-based fusion of thermal and visible imagery, *Computer Vision and Image Understanding* 106 (2-3) (2007) 162–182.
- [41] M. Deshmukh, U. Bhosale, et al., Image fusion and image quality assessment of fused images, *International Journal of Image Processing* 4 (5) (2010) 484.
- [42] J. W. Roberts, J. A. Van Aardt, F. B. Ahmed, Assessment of image fusion procedures using entropy, image quality, and multispectral classification, *Journal of Applied Remote Sensing* 2 (1) (2008) 023522.
- [43] G. Qu, D. Zhang, P. Yan, Information measure for performance of image fusion, *Electronics Letters* 38 (7) (2002) 1.
- [44] H. Chen, P. K. Varshney, A human perception inspired quality metric for image fusion based on regional information, *Information Fusion* 8 (2) (2007) 193–207.
- [45] V. Aslantas, E. Bendes, A new image quality metric for image fusion: The sum of the correlations of differences, *AEU - International Journal of Electronics and Communications* 69 (12) (2015) 1890–1896.
- [46] Z. Wang, A. Bovik, A universal image quality index, *IEEE Signal Processing Letters* 9 (3) (2002) 81–84.
- [47] D. P. Kingma, J. Ba, Adam: A method for stochastic optimization, *arXiv: Learning* (2014).
- [48] H. Zhou, W. Wu, Y. Zhang, J. Ma, H. Ling, Semantic-supervised infrared and visible image fusion via a dual-discriminator generative adversarial network, *IEEE Transactions on Multimedia* (2021).
- [49] W. Zhao, S. Xie, F. Zhao, Y. He, H. Lu, Metafusion: Infrared and visible image fusion via meta-feature embedding from object detection, in: *Proceedings of the IEEE/CVF Conference on Computer Vision and Pattern Recognition*, 2023, pp. 13955–13965.

- [50] H. Li, T. Xu, X.-J. Wu, J. Lu, J. Kittler, Lrrnet: A novel representation learning guided fusion network for infrared and visible images, *IEEE Transactions on Pattern Analysis and Machine Intelligence* (2023).